



Influence of equal channel angular pressing routes on texture, microstructure and mechanical properties of extruded AX41 magnesium alloy



Tomáš Krajňák^{a,*}, Peter Minárik^a, Jenő Gubicza^b, Kristián Máthis^a, Radomír Kužel^a, Miloš Janeček^a

^a Charles University in Prague, Faculty of Mathematics and Physics, Ke Karlovu 3, 121 16 Praha 2, Czech Republic

^b Eötvös Loránd University, Department of Materials Physics, P.O.B. 32, Budapest H-1518, Hungary

ARTICLE INFO

Article history:

Received 13 September 2016

Received in revised form 17 November 2016

Accepted 28 November 2016

Available online 30 November 2016

Keywords:

AX41 magnesium alloy

Equal channel angular pressing routes

Grain size

Dislocation structure

Texture

Proof stress

ABSTRACT

The influence of three different equal channel angular pressing (ECAP) routes (A, Bc and C) on the grain size, texture, dislocation structure and mechanical properties in pre-extruded AX41 magnesium alloy was investigated. It was found that during the first passes, the rate of grain fragmentation strongly depends on the processing route. After 8 passes, despite the almost identical values of the dislocation density ($0.7 \times 10^{14} \text{ m}^{-2}$), the average grain size varied in the range of 2.0–4.5 μm for the individual ECAP routes. Macroscopic texture measurements revealed a gradual formation of very strong textures, which were significantly different for the various processing routes. The strength and the ductility of the samples were investigated by tensile test carried out parallel to the outgoing channel axis. Route A was found to be the most effective processing route for grain refinement. In tensile tests carried out at room and elevated temperatures, the highest strength was observed for the sample processed via route A for 8 passes, due to the highest texture hardening and the smallest grain size.

© 2016 Elsevier Inc. All rights reserved.

1. Introduction

Magnesium, as the lightest structural material, exhibiting high specific strength and excellent castability, is a very promising candidate for a wide range of structural applications. However, the current use of magnesium alloys is limited to room temperature applications, primarily due to the poor creep resistance at temperatures above 100 °C. The low formability of magnesium alloys and strong plastic anisotropy are another issues, which also hinder their wider applications [1,2].

In order to extend the use of magnesium alloys from the room temperature to high temperature applications, several die-cast alloys were developed based on the Mg–Al system by the addition of silicon, zinc, rare earth elements (Nd, La, Ce) and alkaline earths metals (Ca, Sr) [3–5]. The addition of these elements caused the formation of new, thermally stable intermetallic phases, resulting in enhanced creep strength [6]. New ternary magnesium alloy of AX(Mg–Al–Ca) series were developed as cheaper alternative to the alloys containing rare earth alloying elements. These materials exhibit improved high temperature strength and creep resistance due to the presence of Mg₂Ca and Al₂Ca precipitates [7–9].

Processing of magnesium alloys by methods of severe plastic deformation (SPD) was found to be successful for producing of ultrafine-grained microstructures [10,11]. In the last two decades, processing by

equal channel angular pressing (ECAP) becomes the most popular SPD technique [12]. In this method, a sample in the form of a rod or a bar is repeatedly pressed through a die, consisting of two intersecting channels with the same cross section. Various experimental parameters of ECAP processing (the magnitude of the imposed strain, the temperature and the velocity of pressing, the processing route, etc.) significantly influence the microstructural features and mechanical properties of magnesium alloys [13–15]. Generally, ECAP-processed Mg alloys exhibit a strong texture, which is responsible for decreasing the yield stress and enhancing the ductility, despite the significant grain refinement [16–18]. The formed textures depend on the type of deformation route, which is characterized by the angle and direction of the sample rotation between the consecutive passes [19].

The present paper studies a ternary AX41 magnesium alloy processed by a combination of hot extrusion and ECAP. The influence of deformation routes A, Bc and C on grain fragmentation, dislocation density evolution in different slip systems, formation of individual textures and mechanical properties was investigated. A model describing the texture evolution during ECAP processing was also proposed.

2. Experimental Procedures

AX41 magnesium alloy with the composition of Mg – 4 wt.% Al – 1 wt.% Ca was used in this investigation. First, the samples were extruded at 350 °C and a speed of 60 mm/min with an extrusion ratio of 19:1. Billets with the dimensions of 10 × 10 × 100 mm³ were machined from

* Corresponding author.

E-mail address: tomas.krajnak@karlov.mff.cuni.cz (T. Krajňák).

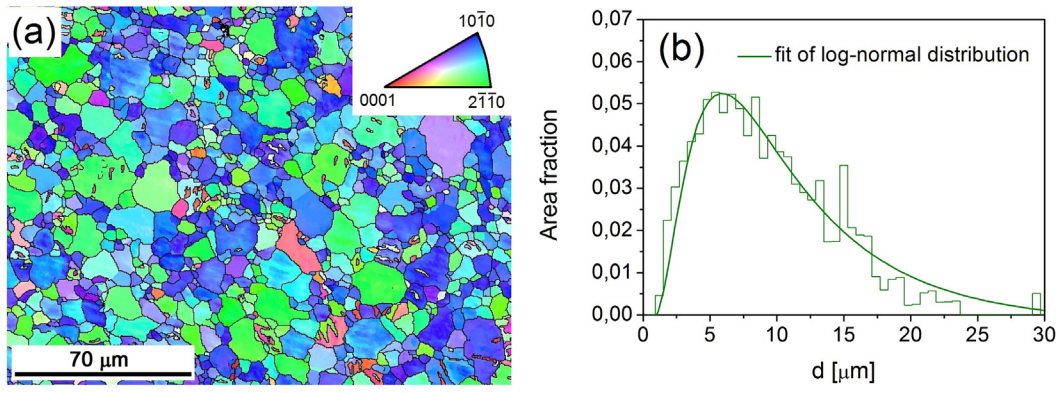


Fig. 1. (a) Inverse pole figure map and (b) grain size distribution of the extruded alloy fitted by a log-normal function.

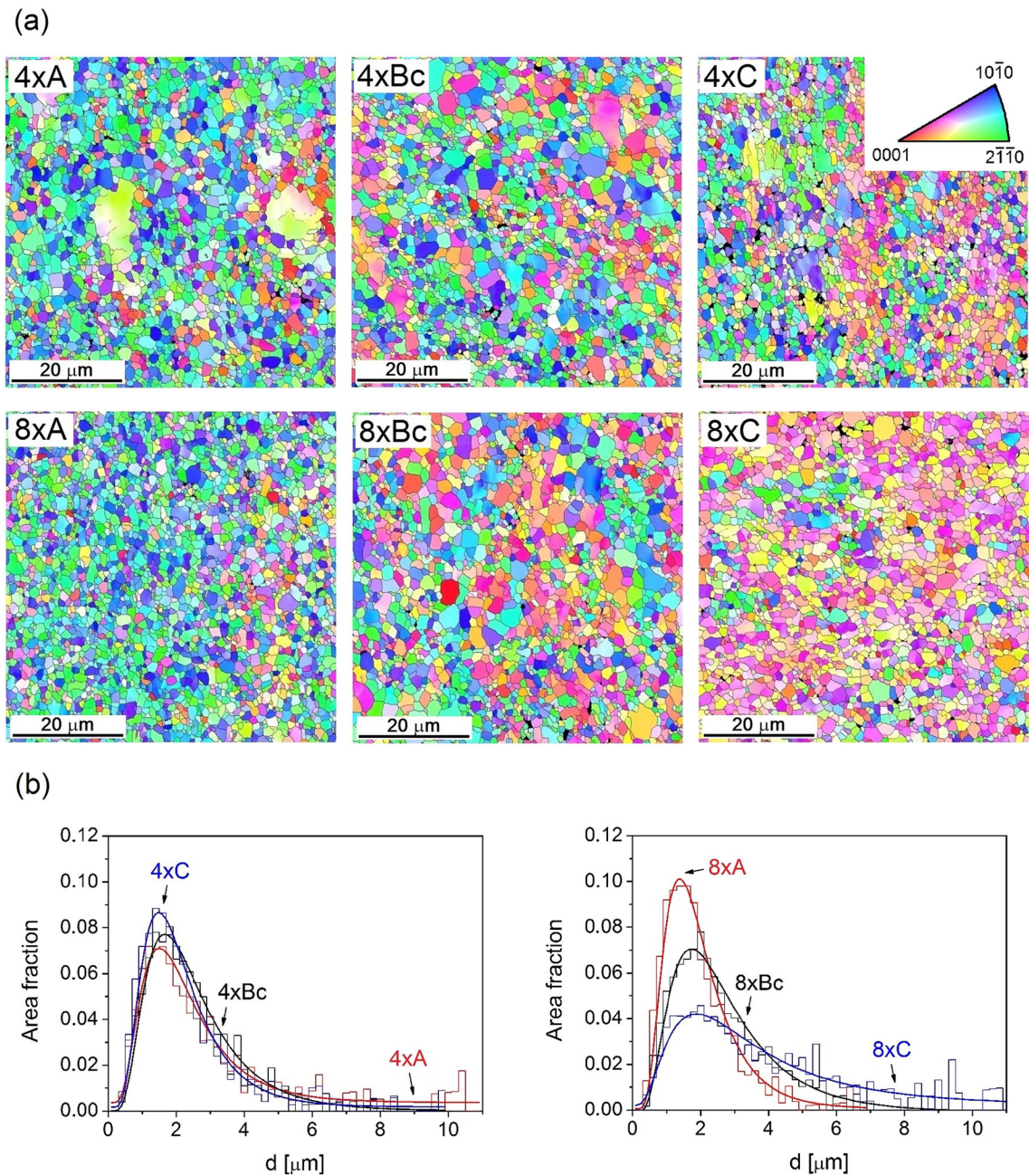


Fig. 2. (a) Inverse pole figure maps obtained on the cross sections and (b) grain size distributions of the samples processed by different deformation routes for 4 and 8 ECAP passes.

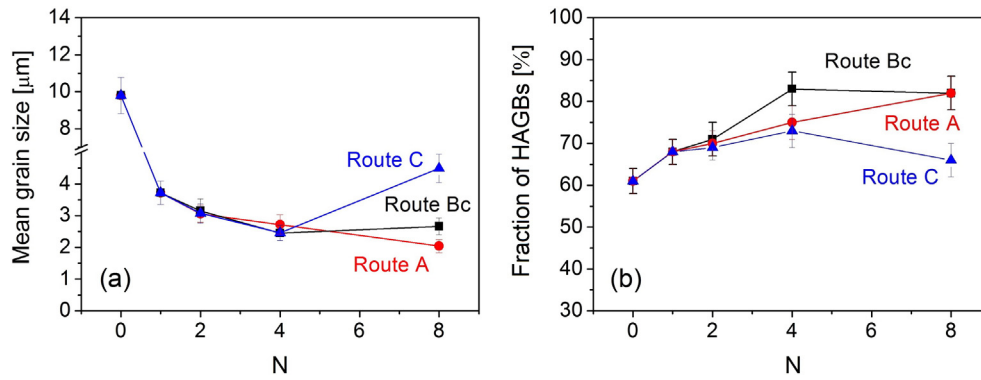


Fig. 3. The dependence of (a) the mean grain size and (b) the fraction of HAGBs on the number of ECAP passes (N) and the route of processing.

the extruded rod. The samples were processed by ECAP at the temperature of 220 °C up to 8 passes, following routes A, Bc and C [20]. All samples were pressed at the speed of 20 mm/min through a die consisting of rectangular channels (inner angle $\phi = 90^\circ$, outer curvature $\psi = 0^\circ$) with the same cross section of $10 \times 10 \text{ mm}^2$. For simplicity, the samples were labeled according to the number of the applied ECAP passes and the route of processing. For instance, the specimen processed by 8 passes using route Bc is labeled as 8xBc.

Microstructural features of the SPD-processed AX41 magnesium alloys were characterized by electron back-scatter diffraction (EBSD) and X-ray line profile analysis (XLP). The samples for all measurements were cut from the rods perpendicular to the pressing direction (plane X [21]) and polished to a mirror like quality using diamond suspensions down to 0.25 μm. Final surface treatment for EBSD was performed by ion polishing using a Gatan PIPS™ ion mill at 2 kV and the incidence angle of 4°. The examination of microstructures was carried out by a Quanta FEG scanning electron microscope operated at 10 kV. Areas of approximately $300 \times 250 \text{ μm}^2$ and $100 \times 100 \text{ μm}^2$ with step sizes of 300 nm and 100 nm for extruded and ECAP-processed samples, respectively, were investigated by EBSD. Measured EBSD data were cleaned using one step of confidence index standardization and two steps of grain dilatation. Further, only points having confidence index >0.1 were used. Before X-ray diffraction experiments, the surface of the samples was etched by a solution of 10 ml acetic acid, 4.2 g picric acid, 10 ml H₂O and 70 ml of ethanol for 20 s in order to remove the surface layer affected by mechanical polishing. The X-ray diffraction spectra were recorded using a high-resolution rotating anode diffractometer (type: RA-MultiMax9, manufacturer: Rigaku) using CuK_{α1} (wavelength: $\lambda = 0.15406 \text{ nm}$) radiation. A narrow parallel X-ray beam with the size of $2 \times 0.2 \text{ mm}^2$ was used in the experiments. Two-dimensional imaging plates detected the Debye-Scherrer diffraction rings. The line profiles were determined as the intensity distribution perpendicular to the rings obtained by integrating the two dimensional intensity distribution along the rings. The X-ray diffraction patterns were evaluated by the Convolutional Multiple Whole Profile (CMWP) fitting method [22]. Nineteen peaks of Mg were used in the fitting procedure, which cover an angular range of diffraction of about 30–135°. Macroscopic crystallographic textures were determined by a Philips X'Pert PRO MRD X-ray diffractometer, using CuK_α radiation ($\lambda = 0.15418 \text{ nm}$), polycapillary in the primary beam, Eulerian cradle, parallel plate collimator and monochromator in the diffracted beam. The pole figures for reflections 0002, 10 $\bar{1}$ 0, 10 $\bar{1}$ 1 and 10 $\bar{1}$ 3 were measured. The average collection time per one pole figure was 5 h. The data evaluation - background correction, orientation distribution function (ODF) calculation and pole figure plotting - was performed by a Philips X'Pert Texture 1.0a software.

Mechanical properties were investigated by tensile tests at 20, 100 and 200 °C. Additional microhardness measurements were carried out at room temperature. The tensile tests were performed at a constant strain rate of 10^{-4} s^{-1} by a universal Instron 5882 testing machine on

specimens with rectangular cross-section of $6 \text{ mm} \times 1 \text{ mm}$ and gauge length of 13 mm. The tensile axis of the samples was parallel to the longitudinal axis of the ECAP-processed billets. The proof stress was determined from the true stress - true strain data at the plastic strain of 0.2%. The Vickers microhardness was measured using an automatic microhardness tester Qness Q10a by applying a load of 100 g for 10 s and taking an average over 30 separate hardness measurements.

3. Experimental Results

3.1. Microstructural Observations by EBSD

The microstructure of the extruded alloy consists of equiaxed grains with log-normal grain size distribution in the range of 1–30 μm, as shown in Fig. 1. In this evaluation only grains with the misorientation angle larger than 15° were considered. Processing by ECAP caused substantial refinement of the extruded microstructure. The fragmentation rate and the final grain size differ for the individual ECAP routes. Homogeneous ultrafine-grained microstructures were formed already after 4 passes via routes Bc and C, whereas in the case of route A this occurs only after 8 passes, cf. Fig. 2a. The grain size distributions obtained as the area fraction of grains versus grain size for the specimens processed by 4 and 8 ECAP passes are shown in Fig. 2b. For all samples, the grain size distribution has approximately a log-normal shape. For routes Bc and C, a broadening of the size distribution towards larger grain sizes was observed between 4 and 8 passes. On the other hand, for route A the grain size distribution became narrower between 4 and 8 passes which was accompanied by a grain refinement.

The mean grain size determined by EBSD from the area fraction calculations for different ECAP routes is plotted in Fig. 3a. It is obvious, that the mean grain size decreased with increasing number of ECAP passes (N) up to 4 passes, irrespectively of the processing route. However, between 4 and 8 passes of ECAP via route A the grain size was further reduced to the value of ~2 μm which contrasts with route Bc, where the grain size remained unchanged ~2.7 μm and route C, where it increased to ~4.5 μm. In Fig. 3b the influence of the number of passes on the fraction of high angle grain boundaries (having the misorientation > 15°)

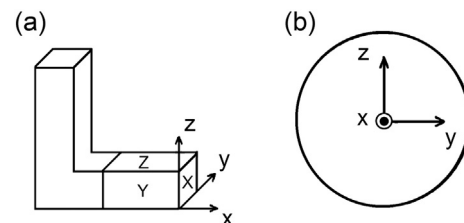


Fig. 4. (a) Notation of axes and planes in the sample coordinate system and (b) the orientation of pole figures.

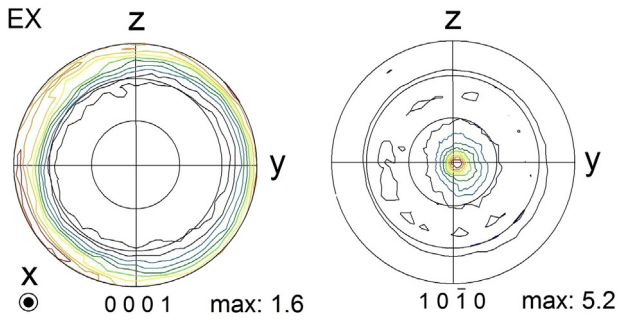


Fig. 5. (0001) and 1010 X-ray pole figures for the extruded sample.

for different processing routes is shown. For all ECAP routes, the fraction of HAGBs gradually increased up to 4 passes. This increment was the most significant for route Bc, where the fraction of HAGBs reached 82%. Similar value was observed for route A only after 8 passes. The fraction of HAGBs for route C was lower than for the other two routes (about 66%).

3.2. Texture Development Investigated by EBSD and X-ray Diffraction

The sample coordinate system (x-, y- and z-axes) and the three orthogonal planes X, Y and Z used for the representation of texture measurements are depicted in Fig. 4a. The x-axis is parallel to the pressing or extrusion direction in the ECAP-processed or extruded sample, respectively. The orientation of the pole figures is displayed in Fig. 4b.

As shown in Fig. 5, the extruded sample exhibits a fiber texture, where the basal planes are orientated parallel to the x-axis. Evenly distributed maximum around the edge of (0001) pole figure indicates that basal planes are randomly rotated around the x-axis. The observed texture is typical for magnesium alloys processed by hot extrusion [23,24]. The (0001) pole figures for the samples processed by different numbers of passes via route A are shown in Fig. 6a. After the first pass of ECAP the original extruded texture was considerably modified and two strong texture components were formed. In the first texture component (denoted as A) the basal planes are parallel to plane Z. In the second texture component (denoted as B) the basal planes are lying parallel to the theoretical shearing plane activated during ECAP [20], i.e., the basal planes are tilted by ~45° to the pressing direction (x-axis). These two texture components were preserved up to the fourth ECAP pass. From the fourth pass via route A, a gradual strengthening of texture component A at the expense of component B can be observed. Thus, after 8 passes the microstructure exhibits a dominant A texture component. Processing of samples via route C up to the fourth pass led to a gradual formation of both texture components A and B (see Fig. 6b). However, after 8 passes the texture component A almost disappeared and only the component B was present. The texture evolution during processing via route Bc is shown in Fig. 6c. From the second pass, the microstructure exhibits both texture components A and B. However, the component B is additionally tilted roughly by 40° towards the y-axis.

In order to compare the microtexture obtained from EBSD measurements with the macrotexture, the pole figures determined by X-ray diffraction for the samples processed by eight passes are summarized in Fig. 7a. It can be concluded, that the pole figures obtained by both techniques (EBSD and X-ray diffraction) are fully consistent. For completing

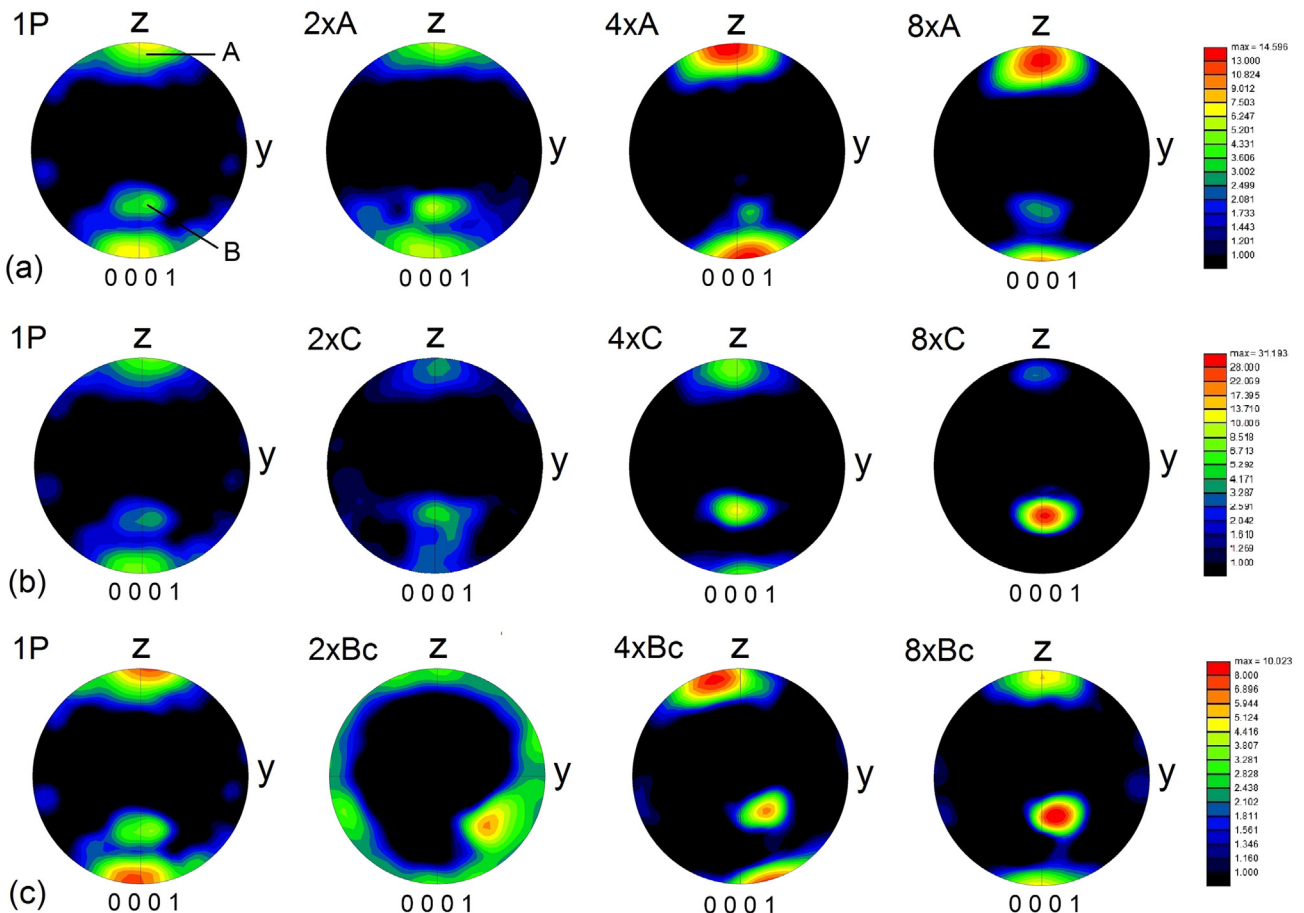


Fig. 6. (0001) EBSD pole figures for samples processed by (a) route A, (b) route C and (c) route Bc.

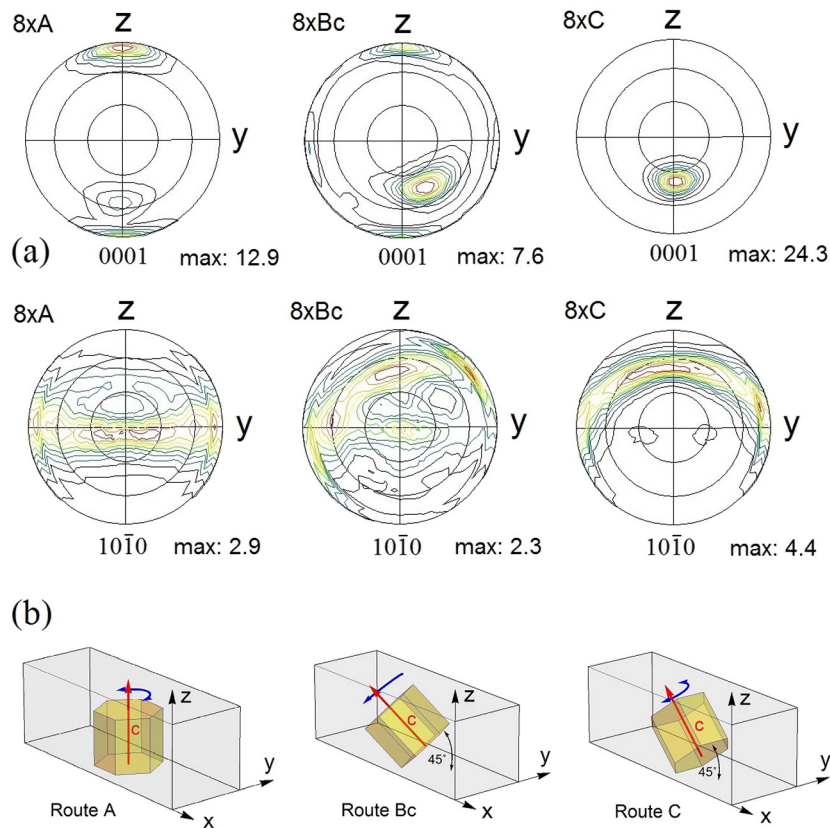


Fig. 7. (a) (0001) and (10 $\bar{1}0$) X-ray pole figures for the samples processed by 8 passes via various deformation routes and (b) graphical representations of the orientation of hexagonal cells for the main texture components in these samples (the random rotation of the prismatic planes around the crystallographic c-axis is marked by the blue arrow). (For interpretation of the references to color in this figure legend, the reader is referred to the web version of this article.)

the texture investigation, the 10 $\bar{1}0$ X-ray pole figures are also plotted in Fig. 7a. The prevailing orientations of the hexagonal cells in specimens processed by 8 passes via different deformation routes are graphically shown in Fig. 7b, where the random rotation of the prismatic planes around the crystallographic c-axis is marked by the blue arrow.

3.3. Microstructural Investigation by XLP

The area-weighted mean crystallite size was calculated according to the formula [22]:

$$\langle x \rangle_{area} = m \times \exp(2.5\sigma^2), \quad (1)$$

where m and σ^2 represent the median and the log-normal variance of the log-normal size distribution function, respectively. The dependence

of the dislocation density (ρ) and the area-weighted mean crystallite size on the number of ECAP passes are plotted in Fig. 8. Note that for the extruded sample the crystallite size and the dislocation density were larger and smaller, respectively, than the detection limits of XLP method (10^{13} m^{-2} for the dislocation density and 1000 nm for the crystallite size). Therefore, these limits were plotted for the extruded specimen in Fig. 8. It is obvious that the area-weighted mean crystallite size and the dislocation density do not depend significantly on the processing route. During the first pass of ECAP the dislocation density significantly increased. Further processing led to the decrease of dislocation density, which is a consequence of the dynamic recovery operating at higher strains [25]. From the fourth pass the dislocation density remained constant within the experimental error which can be attributed to the balance between multiplication and annihilation of dislocations. The crystallite size significantly decreased already after 1 pass to

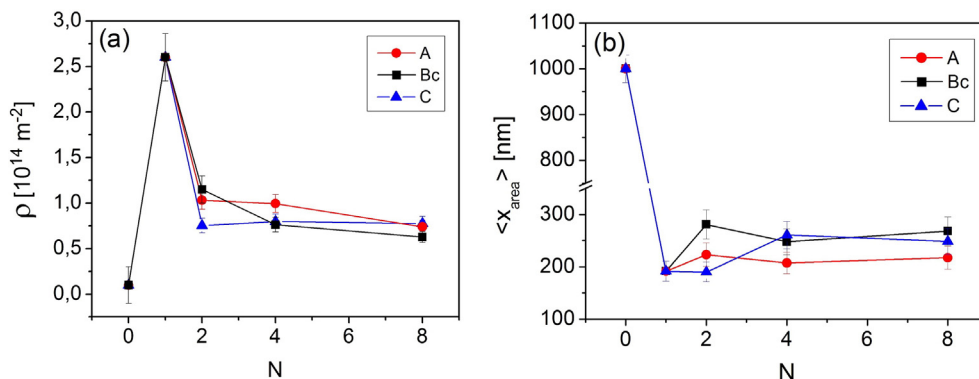


Fig. 8. Dependence of (a) dislocation density and (b) crystallite size on the number of ECAP passes and the route of processing.

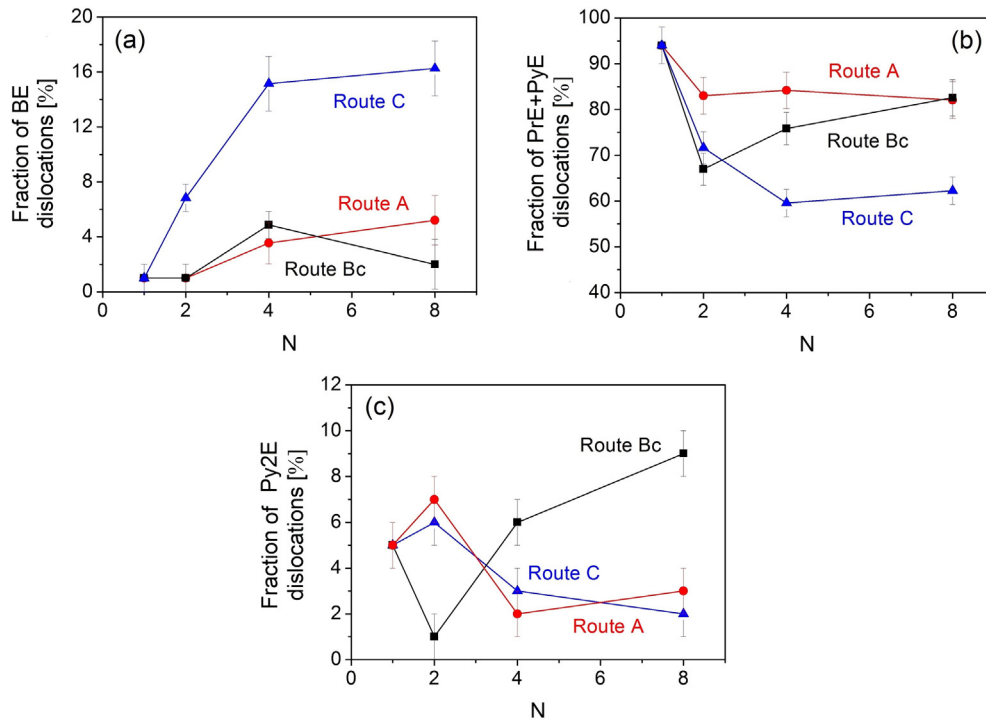


Fig. 9. The dependence of (a) the relative fractions of basal (BE) edge dislocations, (b) the sum of relative fractions of prismatic (PrE) and pyramidal (PyE) <a>-type edge dislocations and (c) the relative fractions of the second order pyramidal edge (Py2E) <c + a> dislocations on the route of ECAP and the number of passes.

the value of ~200 nm. With further straining the crystallite size slightly increased and saturated after 4 passes. In all samples processed by 8 passes the crystallite size was about 250 nm and the dislocation density was approximately $0.7 \times 10^{14} \text{ m}^{-2}$. It is noted that the crystallite size determined from X-ray line profiles is equivalent to the size of coherently scattering domains, which corresponds to dislocations cells or subgrains in SPD-processed metallic materials. Therefore, the crystallite size differs from the grain size determined by EBSD method, which considers only grains with high angle grain boundaries.

In addition to the evaluation of the dislocation density, the analysis of the distribution of dislocations in the particular slip systems was also performed using the procedure described in detail in [26]. As the dislocation contrast factors of X-ray diffraction peaks for prismatic edge (PrE) and pyramidal edge (PyE) dislocations in <a>-type slip system family are close to each other [27], and their separation is difficult, the sum of their fractions is presented only. The majority of dislocations (80–95%) in all ECAP samples have <a>-type Burgers-vector. Fig. 9a, b and c show the fractions of basal edge (BE) and PrE + PyE <a>-type dislocations, as well as the second order pyramidal edge <c + a>

dislocations $\{11\bar{2}2\}\{11\bar{2}\bar{3}\}$ system denoted as Py2E), respectively, as a function of number of ECAP passes for different processing routes. It is apparent from Fig. 9a, that processing via route C led to a higher fraction of BE dislocations in comparison to routes A and Bc. For route C the relative fraction of basal dislocations gradually increased with increasing number of passes and saturated after 4 passes. The relative fraction of basal dislocations for routes A and Bc was the same within the experimental error and only slightly increased with increasing the number of ECAP passes. The sum of fractions of <a>-type PrE and PyE edge dislocations is also strongly depended on the route of processing (see Fig. 9b). Already after the second pass the population of PrE and PyE edge dislocations decrease from 95% to 85% for route A and approximately to 70% for routes Bc and C. The changes in dislocation population between 1 and 2 passes can be explained by the annihilation of dislocations (see Fig. 8a). During further processing via route Bc, the population of PrE and PyE edge dislocations gradually increased to 85%, similar to the value determined for sample 8xA. On the other hand, for route C this population further decreased to 60% after 4 passes of ECAP. From the second pass the relative fraction of Py2E increased during processing

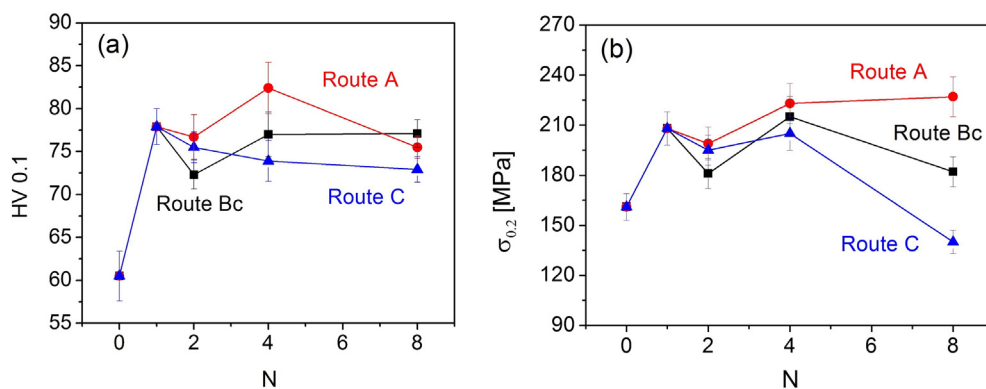


Fig. 10. Evolution of (a) microhardness and (b) proof stress at room temperature with increasing number of ECAP passes for different processing routes.

Table 1

The values of ductility (ϵ_{max}) evaluated from the true stress - true strain curves at room and elevated temperatures.

N	ϵ_{max} [%]								
	20 °C			100 °C			200 °C		
	A	Bc	C	A	Bc	C	A	Bc	C
0	18 ± 3			33 ± 4			50 ± 6		
1	20 ± 4			39 ± 5			130 ± 15		
2	17 ± 3	19 ± 3	22 ± 4	74 ± 8	50 ± 5	69 ± 7	141 ± 20	88 ± 9	156 ± 20
4	15 ± 2	27 ± 4	18 ± 3	45 ± 5	67 ± 7	68 ± 7	90 ± 10	163 ± 20	123 ± 15
8	23 ± 4	23 ± 4	29 ± 4	28 ± 4	66 ± 7	33 ± 4	104 ± 10	175 ± 20	110 ± 12

via route Bc. At the same time, for routes A and C this fraction gradually decreased and saturated after four passes, cf. Fig. 9c.

3.4. Mechanical Properties

The values of the microhardness and the proof stress ($\sigma_{0.2}$) obtained from tensile tests at room temperature are plotted as a function of the number of passes in Fig. 10. It is clearly seen that the evolution of both the microhardness and the proof stress with increasing number of ECAP passes is similar for all processing routes up to the fourth pass. The strength of the samples was significantly improved already after the first pass of ECAP. Further processing up to 4 passes led only to a minor change in the proof stress and the microhardness. After 8 passes, the values of $\sigma_{0.2}$ significantly varied for the different processing routes, in contrast to the values of microhardness, which are the same within the experimental error. As the microhardness test introduces multiaxial loading to the material, the measured values of microhardness are less sensitive to the texture than the proof stress. At the same time, the different behavior of $\sigma_{0.2}$ after 8 passes indicates the effect of texture on mechanical properties. For sample 8xA, the proof stress reached the highest value of 223 MPa. The strength increment due to ECAP was approximately 30% in comparison with the as-extruded state. In specimens processed via routes Bc and C a decrease of proof stress to the values of 180 MPa and 150 MPa, respectively, was observed between 4 and 8 passes. The ductility (ϵ_{max}) measured at room temperature exceeds 15% for all samples, as shown in Table 1.

The variation of the proof stress at elevated temperatures with increasing number of passes is shown in Fig. 11. At the temperature of 100 °C (Fig. 11a), a moderate decrease of the proof stress by about 30–40% in comparison to the room temperature values was observed after 8 passes of ECAP. However, the ductility of these samples increased only slightly, except for 8xBc sample, where ϵ_{max} was approximately 3 times higher than the room temperature value. For $N > 2$, the samples processed via route A exhibit the highest values of $\sigma_{0.2}$. Mechanical

testing at 200 °C (see Fig. 11b) revealed a rapid drop of the proof stress already after the first pass. With further ECAP straining ($N > 2$) $\sigma_{0.2}$ remained approximately unchanged at a level of 20–30 MPa. Significant drop in the proof stress at 200 °C was accompanied by a notable increase in elongation. A maximal ductility of 175% was observed for 8xBc sample. Such an increase in ductility can be explained by a transition in controlling deformation mechanism from the dislocation slip to grain boundary sliding [28].

3.5. Schmid Factors

The values of Schmid factors for uniaxial tension parallel to the x-axis for $\{0001\}\langle 11\bar{2}0 \rangle$ basal, $\{10\bar{1}0\}\langle 11\bar{2}0 \rangle$ prismatic and $\{11\bar{2}2\}\langle 11\bar{2}3 \rangle$ pyramidal slip systems (previously denoted as BE, PrE and Py2E, respectively) were calculated from the experimentally measured texture using the software TSL OIM Analysis 7, and are plotted in Fig. 12. As can be seen from Fig. 12a, the samples processed via route C exhibit the highest values of Schmid factors for basal slip (m_{basal}). Furthermore, m_{basal} increases with increasing number of ECAP passes for routes Bc and C. In contrast, a saturation already after 2 ECAP passes can be observed for route A, which indicates a more difficult activation of basal slip in comparison to other routes. Increasing number of ECAP passes leads to a decrease of Schmid factors for both prismatic (m_{prism}) and the second order pyramidal slips (m_{pyram}) for routes Bc and C. These values remain constant after the first pass for route A and are clearly the highest ones compared to other ECAP routes for 4 and 8 passes.

4. Discussion

4.1. Microstructure

Detailed microstructural observations revealed that processing of extruded AX41 alloy by ECAP via different processing routes led to a gradual microstructure refinement and the formation of a very strong texture. The rate of the microstructure fragmentation is highly affected by the route of processing. Route Bc was found as the most effective way in the formation of homogeneous microstructure with the largest fraction of high angle grain boundaries. Such finding is consistent with the observations performed on many other materials [29,30]. In routes Bc and C, a complete microstructure refinement was observed already after 4 passes, with HAGBs fractions of ~82% and ~72%, respectively. In contrast, for route A grain refinement continues up to 8 passes, resulting in a grain size of ~2 μm . The fraction of HAGBs is ~82%, similar to route Bc.

The process of microstructure refinement in magnesium alloys consists of the nucleation and growth of fine grains along the preexisting grain boundaries [31]. Such formation of grains is attributed to the evolution of stress concentrations at grain boundaries, which causes the

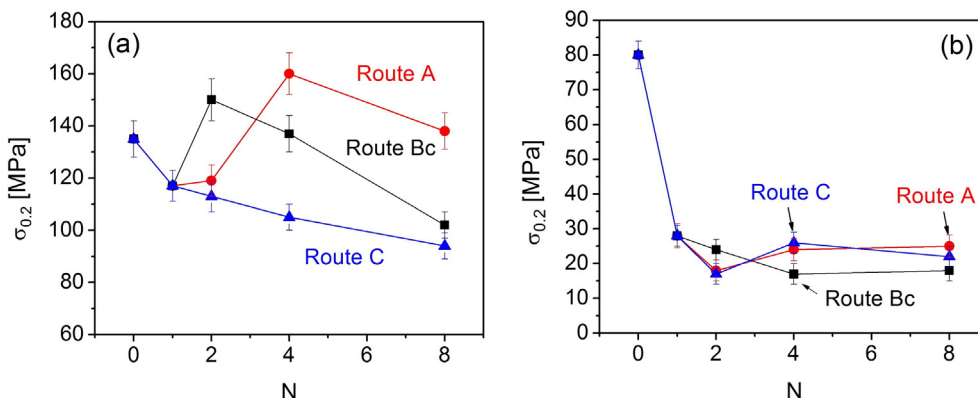


Fig. 11. Evolution of the proof stress (a) at 100 °C and (b) at 200 °C with increasing number of ECAP passes for different processing routes.

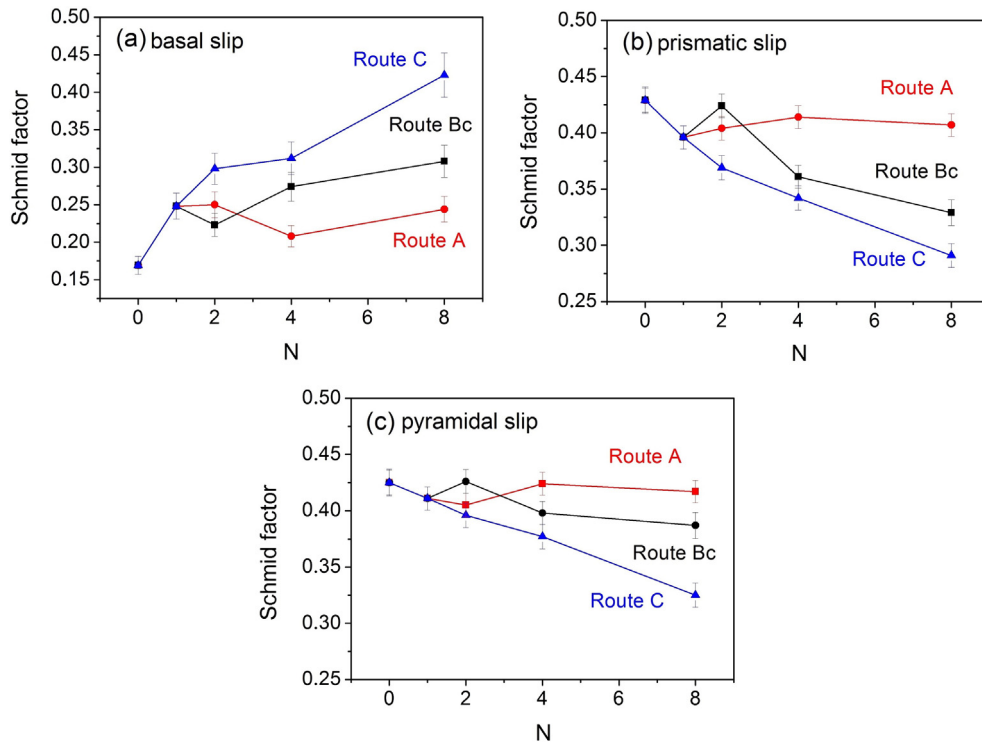


Fig. 12. Dependence of Schmid factors for (a) basal $\langle a \rangle$ slip, (b) prismatic $\langle a \rangle$ slip and (c) the second order pyramidal $\langle c + a \rangle$ slip on the number of ECAP passes and the route of processing.

simultaneous activation of both basal and non-basal slips [32]. Nevertheless, significant difference in the grain size evolution after four passes was observed in routes A and C. The analysis of Burgers vectors population in the samples processed by route A revealed the highest fraction of non-basal dislocations (prismatic (PrE) and pyramidal (PyE) $\langle a \rangle$ -type edge dislocations). This significant activity of non-basal $\langle a \rangle$ -dislocations is in good qualitative agreement with theoretical calculations of Agnew [33] and Li [34]. Modelling results in [33] predict that approx. 20% of strain is accommodated by prismatic $\langle a \rangle$ -slip. Both Li and Agnew further predicted activity of pyramidal $\langle c + a \rangle$ -slip, which is consistent with our observations. The non-basal $\langle a \rangle$ -dislocations have higher probability to lock each other and form dislocation tangles even in small grains, compared to the basal ones. Consequently, the development of new nuclei at the grain boundaries is more probable for higher fractions of non-basal slip systems. During ECAP, the grains formed due to the recrystallization grow with further straining (increasing the number of passes). At the same time, new grains may also nucleate at the boundaries of these growing grains. If grain refinement and coarsening are in equilibrium, the grain size reaches its saturation value. However, for route C the reduced fraction of non-basal dislocations after 4 passes decreased the probability of new grain nucleation during further processing and an increase of the grain size was

observed. Due to the reduced dynamic recrystallization between 4 and 8 passes for route C, the fraction of HAGBs after 8 passes is smaller for this route than for routes A or Bc.

4.2. Texture

The texture formed in ECAP-processed AX41 alloy strongly depends on the deformation route. The identical texture types were also observed in the pre-extruded [35] and the hot-rolled [36] AZ31 magnesium alloys processed by 4 passes via all three deformations routes (A, Bc and C) at temperatures of 250 °C and 220 °C, respectively. Moreover, the same route dependence of texture with increasing number of ECAP passes was observed in the pure magnesium processed at 250 °C [37]. On the other hand, ECAP processed magnesium alloys with Li addition: LAE442 (route Bc) [38] and Mg4L (route A) [33], exhibit distinct texture evolution. It was attributed to the substantial decrease of c/a ratio due to the lithium solved in the Mg matrix, which enhances the activation of $\{10\bar{1}0\}\{11\bar{2}0\}$ prismatic and $\{11\bar{2}2\}\{11\bar{2}3\}$ pyramidal slip systems.

A detailed inspection of the results of texture measurements indicates that the gradual texture formation is related to the grain refinement. It was found that the texture evolution in small ($d < 2 \mu\text{m}$) and

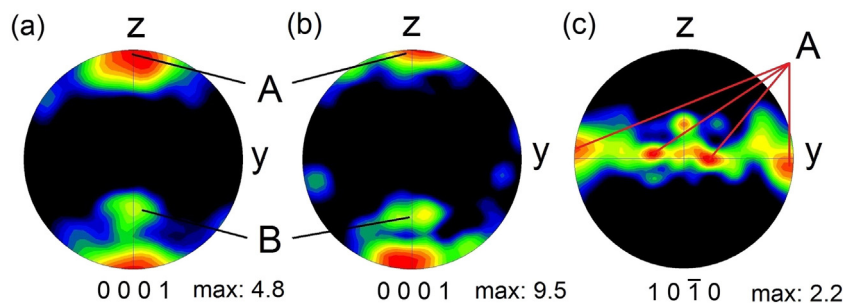


Fig. 13. The EBSD (0001) pole figures corresponding to grains (a) $d < 2 \mu\text{m}$, (b) $d > 2 \mu\text{m}$ and (c) the EBSD $\{10\bar{1}0\}$ pole figure including all grains in the sample processed by 1 pass.

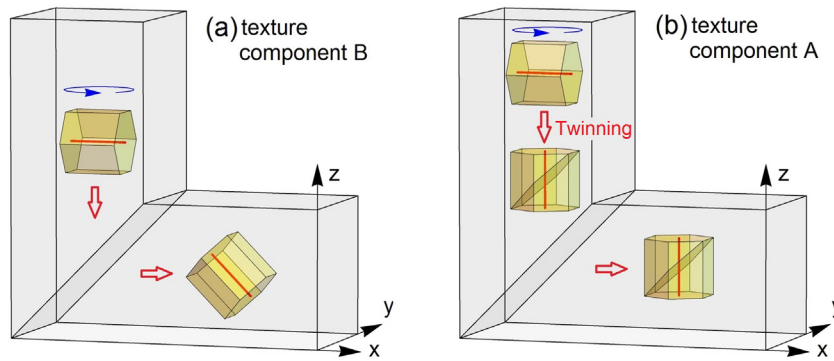


Fig. 14. Schematic representation of formation of (a) texture component B and (b) texture component A during the 1st pass of ECAP.

large grains ($d > 2 \mu\text{m}$) are different, therefore in the following their contributions to the pole figures are considered separately. Fig. 13a and b present the (0001) pole figures for grains smaller and larger than $2 \mu\text{m}$, respectively, in the sample processed by 1 pass. Only slight differences were observed for the two groups of grains. It is clearly seen that the texture component A dominates over the component B in both pole figures. The formation of texture component B already after the first pass can be explained by the activation of basal slip system, which causes the rotation of the (0001) basal planes parallel to the theoretical shearing plane activated during the first pass (see Fig. 14a). This mechanism was proposed previously by Mukai et al. [23]. Texture component A originates from the combination of twinning in compression, occurring already in the feed-in channel and consequently the activation of the second order pyramidal slip system, by which the pyramidal planes $\{11\bar{2}2\}$ remain orientated parallel to ECAP shearing plane, cf. Fig. 14b. Such orientation of hexagonal cells produces 4 maxima lying on the y axis of the $(10\bar{1}0)$ pole figure including all grains (see Fig. 13c). The presence of compression twinning in the extruded pure magnesium and its alloys was documented by many authors [39,40]. This explanation of the formation of texture component A was provided by Minarik et al. [38]. As the intensity of component A is higher than that of component B for both groups of grains, it can be concluded that the influence of the second order pyramidal slip dominates over the basal for $N = 1$, probably due to the easier twinning activation than the basal slip.

The texture components forming during the ECAP process were simulated by Beausir et al. using VPSC model [41]. Despite the fact that their simulations were performed for pure Mg, and without considering the dynamic recrystallization during the ECAP process, the qualitative agreement between the simulations and our experimental results for routes A and Bc is good. In the case of route C their model predicts well the formation of texture component A, but not the component B.

As it was mentioned above, the basic mechanism of texture formation in magnesium alloys during ECAP consists of the rotation of the slip plane of prevailing slip system parallel to the theoretical shearing plane activated during ECAP. As the individual shearing planes activated during ECAP for $N \geq 2$ varied according to the route of processing (see Fig. 15a) [20], the activation of dislocation slip systems varies for the different routes. The analysis of the distribution of dislocations in the particular slip systems showed, that the evolution of basal dislocation population for route A resembles that for route Bc, cf. Fig. 9a, while the evolution of Py2E dislocations population for route A resembles that for route C, cf. Fig. 9c. The different behavior of BE and Py2E dislocations can be explained by considering the orientation of the shearing planes. As for both routes A and Bc, the shearing planes after the Nth and $(N + 1)$ th passes are not parallel, the basal planes activated during the Nth pass must rotate after the $(N + 1)$ th pass, in contrast to route C, where the shearing planes are parallel and the basal planes remained favorably orientated for slip, cf. Fig. 15b. For $\{11\bar{2}2\}$ pyramidal slip, route A resembles route C since for both cases the crystallites consisting of activated pyramidal slip systems in the Nth pass remain favorably

orientated for pyramidal slip in the $(N + 1)$ th pass, considering twinning due to compression in the feed-in channel (see Fig. 16). At the same time, for route Bc the activation of $\{11\bar{2}2\}$ pyramidal slip systems in the $(N + 1)$ th pass requires crystallite rotation, cf. Fig. 16b. Consequently, the evolution of the relative fraction of Py2E dislocations is similar for routes A and C.

In contrast to the sample processed by 1 pass, the orientation of small and large grains for $N = 2$ significantly varied, cf. Fig. 17. As it is apparent from Fig. 17a showing the texture of grains smaller than $2 \mu\text{m}$, in sample 2xA the texture component A still dominates, in contrast to routes C and Bc, where the intensity of component B increases with increasing strain imposed by ECAP is consistent with the behavior of small grains for $N = 2$. As for route A there is no sample rotation after consecutive passes, the orientation of the hexagonal cell for $N \geq 2$ is similar to that in the specimen $N = 1$ (component A), cf. Fig. 18a. Thus, the process of twinning and the activation of the second order pyramidal slip system is repeated, which leads to the preservation of the texture component A up to the final processing step (8 passes). In the case of route C, the gradual formation of single texture component B can be explained by the increasing activity of basal slip, as already after 1 pass the basal planes belonging to the texture component B are favorably orientated for its activation, cf. Fig. 18b. The enhanced activity of basal slip in route C is consistent with the results of the post-mortem analysis of Burgers vectors population (Fig. 9a). Simultaneous weakening of texture component A was confirmed by decreasing activity of the second order pyramidal slip (Fig. 9c). The mechanism of texture formation during processing via route Bc is similar to that for the route C. However,

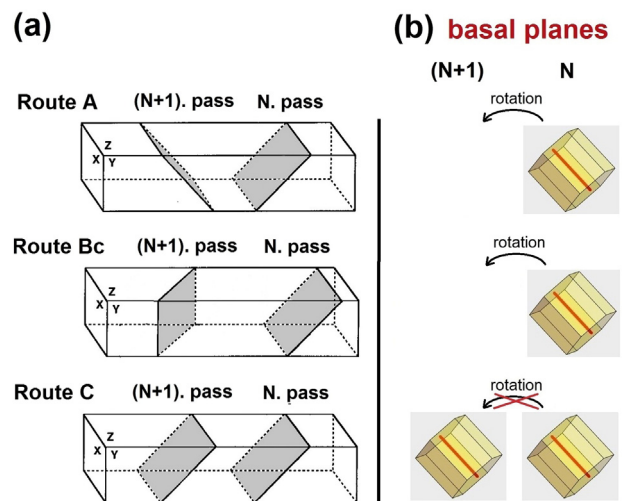


Fig. 15. (a) The shear planes activated during individual ECAP passes performed via different routes and (b) the orientation of slip planes for BE slip systems activated during the various routes.

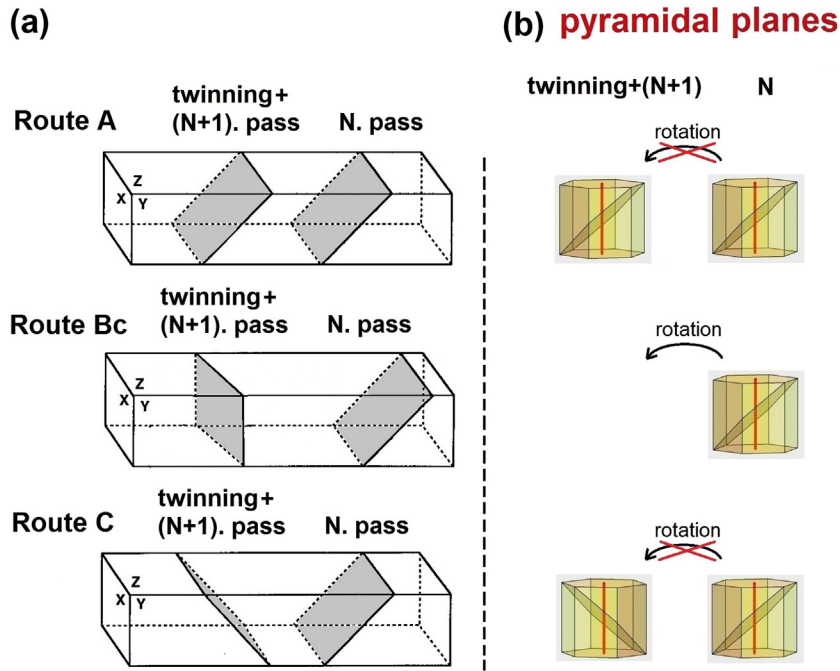


Fig. 16. (a) The shear planes activated during individual ECAP passes performed via different routes, considering the twinning in compression after the Nth pass and (b) the orientation of slip planes for the pyramidal slip systems activated during the various routes.

additional rotation of the texture component B in the 2xBc sample towards the y axis is the result of the billet rotation by 90° between consecutive ECAP passes. In addition, starting from 2 passes via route Bc, the repeated formation of texture component A was observed, as a consequence of increasing activity of the second order pyramidal slip (Fig. 9c).

Above we explained the formation of texture components A and B by the activation of basal and the second order pyramidal slip systems during ECAP. However, the analysis of Burgers vector population performed post-mortem showed that in all ECAP-processed samples the prismatic (PrE) and pyramidal (PyE) edge dislocations have the highest population (see Fig. 9), which was not reflected in the texture observations. This apparent dichotomy can be explained by the difference between the dislocations being active during ECAP-processing and the

remaining dislocations after ECAP. Dislocations gliding through the grains may be annihilated at grain boundaries, therefore they do not contribute to the measured dislocation slip system population [42]. Moreover, the active dislocations may react with each other and form another type of dislocations with reduced activity, thereby causing the difference between the most active and the post-mortem measured dislocation populations.

4.3. Mechanical Properties

From the results of mechanical testing it can be concluded that processing via route A leads to the highest values of $\sigma_{0.2}$ after 8 passes, which contrasts to routes Bc and C, where the highest value of $\sigma_{0.2}$ was obtained already after the 4th pass. In order to discuss the influence

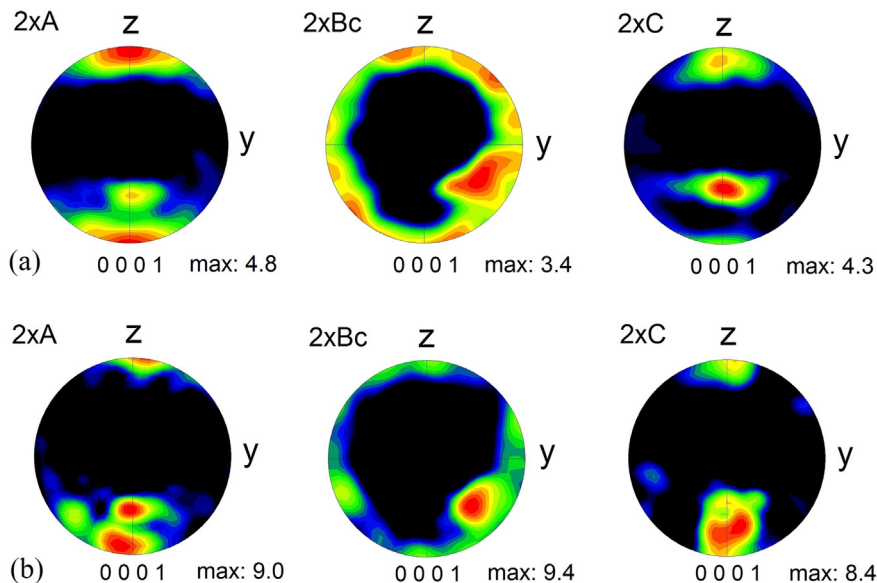


Fig. 17. EBSD (0001) pole figures after 2 passes of ECAP for different routes (a) grains < 2 μm, (b) grains > 2 μm.

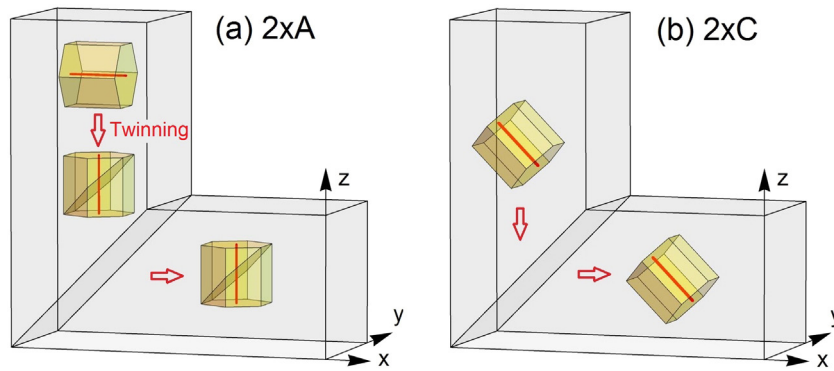


Fig. 18. Schematic representation of the formation of texture during the 2nd pass of ECAP via (a) route A and (b) route C.

of texture and grain size (Hall–Petch) strengthening on $\sigma_{0.2}$, the strength increment caused by dislocations was subtracted from the measured proof stress. The dislocation hardening was calculated according to the Taylor formula as:

$$\sigma_D = \alpha M^T G b \rho^{1/2} \quad (2)$$

where G is the shear modulus (17 GPa [43]), b is the average length of the Burgers vector calculated according to the fractions of the different slip systems, and ρ is the dislocation density. As the Taylor factor M_T and dislocation–dislocation interaction constant α depend on the texture and the activated slip system, different values of these parameters were used for individual samples. The parameter α varies in the range between 0.2 for basal–basal interaction to a maximum of 1.9 for basal–pyramidal interaction [44]. For the samples where larger participation of basal slip was assumed (i.e., for route C), the M_T was selected to be about 4.5 [45] and $\alpha \approx 0.3$, reflecting the basal–basal interaction. For samples processed via route Bc, where balanced mixture of basal, prismatic and pyramidal slip can be assumed, the M_T was selected to be about 2.5 [45] and $\alpha \approx 0.6$, as these values are the average of the basal–basal and basal–prismatic interaction constants. For samples inhibiting basal and prismatic slip while favoring pyramidal polyslip (route A), M_T was about 2.1 [45] and $\alpha \approx 0.8$, representing the average of the basal–basal, basal–prismatic and basal–pyramidal interaction constants. The dependence of the proof stress reduced by dislocation hardening, denoted as $(\sigma_{0.2} - \sigma_D)$, on the number of ECAP passes for all deformations routes is plotted in Fig. 19.

For all deformation routes, a gradual increase of reduced proof stress $(\sigma_{0.2} - \sigma_D)$ up to 4 passes is observed, which is consistent with the grain refinement, cf. Fig. 3a. The difference in the proof stress after 8 passes for various routes can be attributed to different grain sizes and textures. The higher grain size for 8xC sample in comparison with 8xA and 8xBc

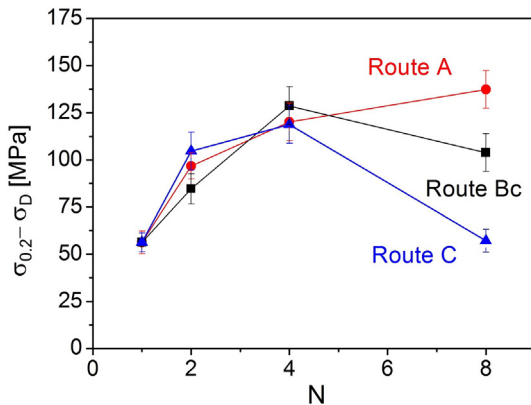


Fig. 19. Evolution of the reduced proof stress at room temperature with increasing number of ECAP passes for different processing routes.

specimens contributes to the lower proof stress. The texture influences the proof stress via the variation of Schmid factors of the different slip systems as a function of routes and number of passes, as shown in Fig. 12. The increasing value of Schmid factors for basal slip between 4 and 8 passes for routes Bc and C yields a softening of these specimens (see Fig. 10b). After 8 passes, softening due to the texture change overwhelmed the strengthening owing to grain size refinement and a decrease in the reduced proof stress can be observed. As a consequence, the proof stress of the 8xC sample is similar to that after extrusion. This observation is consistent with the common finding in the literature, where the decrease of the proof stress was usually explained by texture softening [10,36]. In contrast, the Schmid factors for basal, prismatic and pyramidal slip systems for the samples processed by route A are approximately constant for $N > 1$. As a consequence, the contribution of the texture to softening/hardening remains practically unchanged. For the samples processed by route A, the Schmid factor for basal slip is the lowest compared to other routes, therefore the activation of basal slip during tensile test is much more difficult. On the other hand, the values of Schmid factors for prismatic and the second order pyramidal slip systems are the highest for route A. As the orientation of grains is not suitable for twinning during tension along the x-axis after ECAP, the higher probability of activation of non-basal slip systems and the interaction of non-basal dislocation with basal ones caused additional hardening. Contrary to specimens 8xBc and 8xC, the reduced proof stress $(\sigma_{0.2} - \sigma_D)$ for sample 8xA increases between 4 and 8 passes as a result of further grain refinement. Finally, it can be concluded that the proof stress reduction for routes Bc and C between 4 and 8 passes can be attributed to texture softening.

The evolution of $\sigma_{0.2}$ with increasing N at 100 °C strongly depends on the ECAP route and is consistent with the evolution of Schmid factors for basal slip. It indicates that the observed reduction of $\sigma_{0.2}$ at 100 °C in comparison to the room temperature values can be mainly attributed to the increasing activation of basal slip. The similar prominent role of the basal slip during high-temperature deformation was also observed in microcrystalline pure Mg [46].

5. Conclusions

The influence of deformation routes A, Bc and C of ECAP processing on the development of microstructure, texture and mechanical properties in extruded AX41 alloy was studied. The following conclusions can be drawn from this investigation:

1. The highest refinement of the microstructure was achieved after 8 passes via route A, where the mean grain size decreased to 2 μm and the fraction of high angle grain boundaries reached 82%.
2. The crystallite size and density of dislocations was not affected by the deformation routes. After 8 passes of ECAP, the crystallite size and the dislocation density were about 220 nm and $0.7 \times 10^{14} \text{ m}^{-2}$, respectively.

3. The texture was found to be significantly influenced by the processing route. In all samples, two main texture components were formed, but their intensities were different for the different ECAP routes. As a consequence, the Schmid factors for individual slip systems were also different. The samples processed via routes Bc and C for 8 passes exhibited high tendency for basal slip in tensile tests carried out parallel to the longitudinal axis of the billets. In contrast, the activation of non-basal slip systems during tension was the easiest in the sample processed by route A.
4. In room temperature tension, the highest proof stress (~227 MPa) was achieved for sample 8xA, as a consequence of the significant texture hardening and the substantial grain size reduction. The ductility was between 20 and 30% for all routes. At 100 °C, the sample 8xA exhibited the highest strength (~140 MPa) among the specimens processed by the three routes. At 200 °C, a strong strength degradation to 20–30 MPa was found for all specimens, while the ductility was enhanced to 100–175%.
5. Route A was found to be the most effective processing route for extruded AX41 magnesium alloy from the viewpoint of both grain refinement and mechanical properties.

Acknowledgement

This work was financially supported by the Czech Science Foundation under the project P107/13/13616S. J.G. acknowledges the financial support of the Hungarian Scientific Research Fund, OTKA, Grant no. K-109021.

References

- [1] M. Masoumi, H. Hu, Influence of applied pressure on microstructure and tensile properties of squeeze cast magnesium Mg-Al-Ca alloy, *Mater. Sci. Eng. A* 528 (2011) 3589–3593.
- [2] E. Yukutake, J. Kaneko, M. Sugamata, Anisotropy and non-uniformity in plastic behavior of AZ31 magnesium alloy plates, *Mater. Trans.* 44 (2003) 452–457.
- [3] M.O. Pekguleryuz, A.A. Kaya, Creep resistant magnesium alloys for powertrain applications, in: K.U. Kainer (Ed.), *Magnesium Alloys and Their Applications*, Wiley-VCH Verlag GmbH, Weinheim 2003, pp. 74–93.
- [4] A.A. Luo, Recent magnesium alloy development for automotive powertrain applications, *Mater. Sci. Forum* 419–422 (2003) 57–66.
- [5] I.A. Anyanwu, Y. Gokan, A. Suzuki, S. Kamado, Y. Kojima, S. Takeda, T. Ishida, Effect of substituting cerium-rich mischmetal with lanthanum on high temperature properties of die-cast Mg-Zn-Al-Ca-RE alloys, *Mater. Sci. Eng. A* 380 (2004) 93–99.
- [6] A. Suzuki, N.D. Saddock, J.W. Jones, T.M. Pollock, Solidification paths and eutectic intermetallic phases in Mg-Al-Ca ternary alloys, *Acta Mater.* 53 (2005) 2823–2834.
- [7] R. Ninomiya, T. Ojio, K. Kubota, Improved heat resistance of Mg-Al alloys by the Ca addition, *Acta Metall. Mater.* 43 (1995) 669–674.
- [8] Y. Terada, R. Sota, N. Ishimatsu, T. Sato, K. Ohoi, A thousandfold creep strengthening by Ca addition in die-cast AM50 magnesium alloy, *Metall. Mater. Trans. A* 35 (2004) 3029–3032.
- [9] M.O. Pekguleryuz, J. Renaud, in: H. Kaplan, J. Hryn, B. Clow (Eds.), *Creep Resistance in Mg-Al-Ca Casting Alloys*, Magnesium Technology, 2000, TMS, Nashville 2000, pp. 279–284.
- [10] H.K. Lin, J.C. Huang, T.G. Langdon, Relationship between texture and low temperature superplasticity in an extruded AZ31 Mg alloy processed by ECAP, *Mater. Sci. Eng. A* 402 (2005) 250–257.
- [11] A. Yamashita, Z. Horita, T.G. Langdon, Improving the mechanical properties of magnesium and a magnesium alloy through severe plastic deformation, *Mater. Sci. Eng. A* 300 (2001) 142–147.
- [12] V.M. Segal, Materials processing by simple shear, *Mater. Sci. Eng. A* 197 (1995) 157–164.
- [13] S. Seipp, M.F. Wagner, K. Hockauf, I. Schneider, L.W. Meyer, M. Hockauf, Microstructure, crystallographic texture and mechanical properties of the magnesium alloy AZ31B after different routes of thermo-mechanical processing, *Int. J. Plast.* 35 (2012) 155–166.
- [14] M. Gzyl, A. Rosochowski, E. Yakushina, P. Wood, L. Olejnik, Route effects in I-ECAP of AZ31B magnesium alloy, *Key Eng. Mater.* 554–557 (2013) 876–884.
- [15] W.J. Kim, S.I. Hong, Y.S. Kim, S.H. Min, H.T. Jeong, J.D. Lee, Texture development and its effect on mechanical properties of an AZ61 Mg alloy fabricated by equal channel angular pressing, *Acta Mater.* 51 (2003) 3293–3307.
- [16] J. Suh, J.V. Hernández, D. Letzig, R. Golle, W. Volk, Effect of processing route on texture and cold formability of AZ31 Mg alloy sheets processed by ECAP, *Mater. Sci. Eng. A* 669 (2016) 159–170.
- [17] S.R. Agnew, J.A. Horton, T.M. Lillo, D.W. Brown, Enhanced ductility in strongly textured magnesium produced by equal channel angular processing, *Scr. Mater.* 50 (2004) 377–381.
- [18] S.R. Agnew, P. Mehrotra, T.M. Lillo, G.M. Stoica, P.K. Liaw, Crystallographic texture evolution of three wrought magnesium alloys during equal channel angular extrusion, *Mater. Sci. Eng. A* 408 (2005) 72–78.
- [19] L.B. Tong, M.Y. Zheng, X.S. Hu, K. Wu, S.W. Xu, S. Kamado, Y. Kojima, Influence of ECAP routes on microstructure and mechanical properties of Mg-Zn-Ca alloy, *Mater. Sci. Eng. A* 527 (2010) 4250–4256.
- [20] M. Furukawa, Z. Horita, M. Nemoto, T.G. Langdon, Review: processing of metals by equal-channel angular pressing, *J. Mater. Sci.* 36 (2001) 2835–2843.
- [21] Y. Iwahashi, J. Wang, Z. Horita, M. Nemoto, T.G. Langdon, The shearing characteristics associated with equal-channel angular pressing, *Mater. Sci. Eng. A* 257 (1998) 328–332.
- [22] G. Ribárik, J. Gubicza, T. Ungár, Correlation between strength and microstructure of ball-milled Al-Mg alloys determined by X-ray diffraction, *Mater. Sci. Eng. A* 387–389 (2004) 343–347.
- [23] T. Mukai, M. Yamanoi, H. Watanabe, K. Higashi, Ductility enhancement in AZ31 magnesium alloy by controlling its grain structure, *Scr. Mater.* 45 (2001) 89–94.
- [24] H.K. Lin, J.C. Huang, High strain rate and/or low temperature superplasticity in AZ31 Mg alloys processed by simple high-ratio extrusion methods, *Mater. Trans.* 43 (2002) 2424–2432.
- [25] J. Müller, M. Janeček, S. Yi, J. Čížek, L. Wagner, Effect of equal channel angular pressing on microstructure, texture, and high-cycle fatigue performance of wrought magnesium alloys, *Int. J. Mater. Res.* 100 (2009) 838–842.
- [26] K. Máthys, K. Nyilas, A. Axt, I.C. Dragomir, T. Ungár, P. Lukáč, The evolution of non-basal dislocations as a function of deformation temperature in pure magnesium determined by X-ray diffraction, *Acta Mater.* 52 (2004) 2889–2894.
- [27] I.C. Dragomir, T. Ungár, Contrast factors of dislocations in the hexagonal crystal system, *J. Appl. Crystallogr.* 35 (2002) 556–564.
- [28] K. Matsubara, Y. Miyahara, Z. Horita, T.G. Langdon, Developing superplasticity in a magnesium alloy through a combination of extrusion and ECAP, *Acta Mater.* 51 (2003) 3073–3084.
- [29] K. Oh-ishi, Z. Horita, M. Furukawa, M. Nemoto, T.G. Langdon, Optimizing the rotation conditions for grain refinement in equal-channel angular pressing, *Metall. Mater. Trans. A* 29 (1998) 2011–2013.
- [30] J. Wongsangam, M. Kawasaki, T.G. Langdon, The development of hardness homogeneity in a Cu-Zr alloy processed by equal-channel angular pressing, *Mater. Sci. Eng. A* 556 (2012) 526–532.
- [31] R.B. Figueiredo, T.G. Langdon, Principles of grain refinement in magnesium alloys processed by equal-channel angular pressing, *J. Mater. Sci.* 44 (2009) 4758–4762.
- [32] A. Galiyev, R. Kaibyshev, G. Gottstein, Correlation of plastic deformation and dynamic recrystallization in magnesium alloy ZK60, *Acta Mater.* 49 (2001) 1199–1207.
- [33] S.R. Agnew, P. Mehrotra, T.M. Lillo, G.M. Stoica, P.K. Liaw, Texture evolution of five wrought magnesium alloys during route a equal channel angular extrusion: experiments and simulations, *Acta Mater.* 53 (2005) 3135–3146.
- [34] S. Li, Orientation stability in equal channel angular extrusion. Part II: hexagonal close-packed materials, *Acta Mater.* 56 (2008) 1031–1043.
- [35] M. Gzyl, A. Rosochowski, R. Pesci, L. Olejnik, E. Yakushina, P. Wood, Mechanical properties and microstructure of AZ31B magnesium alloy processed by I-ECAP, *Metall. Mater. Trans. A* 45 (2014) 1609–1620.
- [36] S.X. Ding, W.T. Lee, C.P. Chang, L.W. Chang, P.W. Kao, Improvement of strength of magnesium alloy processed by equal channel angular extrusion, *Scr. Mater.* 59 (2008) 1006–1009.
- [37] S. Suwas, G. Gottstein, R. Kumar, Evolution of crystallographic texture during equal channel angular extrusion (ECAE) and its effects on secondary processing of magnesium, *Mater. Sci. Eng. A* 471 (2007) 1–14.
- [38] P. Minárik, R. Král, J. Čížek, F. Chmelík, Effect of different c/a ratio on the microstructure and mechanical properties in magnesium alloys processed by ECAP, *Acta Mater.* 107 (2016) 83–95.
- [39] T.Y.E. Sukedai, Investigation of tensile compressive yield asymmetry and the role of deformation twin in extruded pure magnesium, *Int. J. Mater. Res.* 101 (2010) 736–740.
- [40] S.M. Yin, C.H. Wang, Y.D. Diao, S.D. Wu, S.X. Li, Influence of grain size and texture on the yield asymmetry of Mg-3Al-1Zn alloy, *J. Mater. Sci. Technol.* 27 (2011) 29–34.
- [41] B. Beausir, S. Suwas, L.S. Tóth, K.W. Neale, J.J. Fundenberger, Analysis of texture evolution in magnesium during equal channel angular extrusion, *Acta Mater.* 56 (2008) 200–214.
- [42] T. Mayama, M. Noda, R. Chiba, M. Kuroda, Crystal plasticity analysis of texture development in magnesium alloy during extrusion, *Int. J. Plast.* 27 (2011) 1916–1935.
- [43] D.H. Chung, W.R. Buessem, in: F.W. Vahldiek, S.A. Mersol (Eds.), *The Elastic Anisotropy of Crystals, Anisotropy in Single Crystal Refractory Compounds*, vol. 2, Plenum Press, New York 1968, pp. 217–245.
- [44] F.F. Lavrentev, Y.A. Pokhil, S.V. Sokolsky, in: P. Haasen, V. Gerold, G. Kostorz (Eds.), *Strength of Metals and Alloys (ICSM-5)*, Pergamon Press, New York 1979, p. 163.
- [45] C. Caceres, P. Lukáč, Strain hardening behaviour and the Taylor factor of pure magnesium, *Philos. Mag.* 88 (2008) 977–989.
- [46] C.M. Cepeda-Jiménez, J.M. Molina-Aldareguia, F. Carreño, M.T. Pérez-Prado, Prominent role of basal slip during high-temperature deformation of pure Mg polycrystals, *Acta Mater.* 85 (2015) 1–13.